

Spiral Disk Opacity from Occulting Galaxy Pairs in the Sloan Digital Sky Survey

B. W. Holwerda¹, W. C. Keel²

and

A. Bolton³

holwerda@stsci.edu

ABSTRACT

A spiral galaxy partially overlapping a more distant elliptical offers an unique opportunity to measure the dust extinction in the foreground spiral. From the Sloan Digital Sky Survey DR4 spectroscopic sample, we selected 83 occulting galaxy pairs and measured disk opacity over the redshift range $z = 0.0-0.2$ with the goal to determine the recent evolution of disk dust opacity. The enrichment of the ISM changes over the lifetime of a disk and it is reasonable to expect the dust extinction properties of spiral disks as a whole to change over their lifetime. When they do, the change will affect our measurements of galaxies over the observable universe.

From the SDSS pairs we conclude that spiral disks show evidence of extinction to ~ 2 effective radii. However, no evidence for recent evolution of disk opacity is evident, due to the limited redshift range and our inability to distinguish other factors on disk opacity such as the presence of spiral arms and Hubble type. Such effects also mask any relation between surface brightness and optical depth that has been found in nearby galaxies. Hence, we conclude that the SDSS spectral catalog is an excellent way to find occulting pairs and construct a uniform local sample. However, higher resolution than the SDSS images is needed to disentangle the effects of spiral arms and Hubble type from evolution since $z = 0.2$.

¹Space Telescope Science Institute, 3700 San Martin Drive, Baltimore, MD 21218, USA

²Department of Physics and Astronomy, University of Alabama, Box 870324, University of Alabama, Tuscaloosa, AL 35487-0324, USA

³Harvard-Smithsonian Center for Astrophysics, 60 Garden St. MS-20, Cambridge, MA 02138, USA

Subject headings: (ISM:) dust, extinction, galaxies: ISM, galaxies: spiral, galaxies: evolution, galaxies: structure, galaxies: fundamental parameters (disk opacity)

1. Introduction

The role of extinction may well change across the now-observable range of redshifts, as heavy elements are injected into the ISM but the reservoir of gas within a galaxy is progressively cycled through stars. Thus the history of dust within galaxies is intimately linked to the history of the overall star-formation rate, which has been at least partly specified through observations of several deep fields with HST and other instruments. Calzetti & Heckman (1999) incorporated both SFR and abundance constraints to examine the possible histories of galaxy extinction, finding that these constraints allow two classes of solutions. These have markedly different redshift behavior, one with a peak extinction early on ($z \approx 3$), and the other building up dust more gradually with a peak extinction as late as $z = 1$.

The typical dust mass in distant galaxies is very much a function of the selected sample. Far-infrared selected samples point to more Arp-220 like dust prominence (Rowan-Robinson et al. 2005), optical/UV selected samples point to disks very similar to the local ones (Sajina et al. 2006) and Lyman- α galaxies point to low-extinction disks (Nilsson et al. 2007).

The observational situation at large redshifts is still ill-constrained, so far based on (i) modeling the spectral energy distributions (SEDs) of galaxies at high z (Rowan-Robinson 2003; Rowan-Robinson et al. 2005; Sajina et al. 2006; Nilsson et al. 2007), (ii) measuring differences in the SEDs of lensed quasars in which one image is formed deep within the lens system (e.g., Nadeau et al. 1991; Falco et al. 1999; Motta et al. 2002; Elíasdóttir et al. 2006), (iii) correlating the colors of quasars with metal-line absorption systems compared to average QSO SEDs (Hopkins et al. 2004), and (iv) the extinction fits to SN1a lightcurves (e.g., Knop et al. 2003; Jha et al. 2007). To date, the SED models have yielded the most results: Rowan-Robinson (2003) find a peak extinction at $z \sim 1$ and lower beyond that –no extinction at $z = 6-7$ according to Yan et al. (2005). Yet Vijh et al. (2003) find a strong correction for the SFR in the early universe due to dust attenuation by an LMC-type dust. The QSO SED’s match the SMC’s extinction law with most of the extinction in the nucleus itself. Most of the lensing systems are early-types however. Lensing measurements find a wide range in the value of R_V and the SN1a measurements find no change in reddening.

The first three methods are very vulnerable to color and surface brightness selection effects and the SED models are very dependent on the assumed geometry of ISM and stars.

Partially overlapping galaxies offer an alternative and more direct way to approach the question of the evolution of dusty ISM in spirals.

2. The occulting galaxy pairs technique

An occulting galaxy pair –a foreground spiral partially covering a background galaxy– can be used up to high redshift to determine the opacity of the spiral. The flux contributions in the overlap region from both galaxies are estimated from the non-overlap parts (Figure 1). From a single image, we obtain the non-overlapping flux from the foreground spiral (F'), the non-overlap background flux (B') and the flux from the overlap region ($F + Be^{-\tau}$). We can now estimate the optical depth (τ') from these three observables: $e^{-\tau'} = ([F + Be^{-\tau}] - F')/B'$.

As the background galaxy, a partially occulted elliptical is ideal because its light profile is very symmetric: the assumption that the non-occulted part is a good approximation of the occulted part is a reasonable one. This leaves the assumption that the foreground spiral is symmetric as the predominant source of uncertainty. The method has been extensively used in the local universe which gives us a direct comparison set for more distant measurements.

The occulting galaxy technique was originally proposed by White & Keel (1992) to probe spiral disk extinction in the local universe, and in the following decade the known nearby overlapping-galaxy pairs were exhausted, using both ground-based imaging (Andredakis & van der Kruit 1992; Berlind et al. 1997; Domingue et al. 1999; White et al. 2000), spectroscopy (Domingue et al. 2000) and HST/WFPC2 imaging (Keel & White 2001a,b; Elmegreen et al. 2001). The ideal pair, described by White & Keel (1992), is a bright elliptical partially behind a symmetric, face-on spiral. Since only a few pairs were known in the local universe, these studies used a great variety of background galaxies. Their results included radial extinction plots for the extinction across the entire height of the disk. The results follow a gray extinction law when taken over large regions but approaches a typical Galactic extinction law for scales smaller than 100 pc (Keel & White 2001a). Some indication that the cloud sizes are fractal in nature was found by Keel & White (2001a). Holwerda et al. (2005a) used counts of distant galaxies seen in HST images of nearby spirals to independently confirm the values for disk extinction from occulting pairs.

From the SDSS DR4 spectroscopic sample we have selected 83 occulting pairs with an elliptical as the background galaxy –the ideal configuration. The foreground spiral galaxies span a range in redshift ($z=0.01-0.3$). Starting with spectroscopic identification of both sources and their redshifts represents a significant improvement in reliability and quality of the pairs. The ideal occulting pair –spiral over elliptical– provides the best estimate of dust

content of a the spiral disk (Figure 1). An additional advantage of this SDSS sample is a high separation in redshift (Δz) of background and foreground galaxy; there are fewer issues with scatter of background light and interacting pairs.

This SDSS sample has selection properties more like what we are likely to get in the high- z fields than our carefully culled previous overlap sample (carefully culled to reduce the incidence of galaxies with asymmetry issues, for example) and this, while the bulk measurements will have larger errors, is perhaps a better starting point if we want to look for evolution of the disk extinction. Also, this technique, while very likely suboptimal for some individual marginal cases where an analysis “by hand” could do better, is more like what one can try on the large samples of poorly-resolved systems at higher redshift ($z > 0.3$).

3. Sample selection

Warren et al. (1996); Bolton et al. (2004) describe a technique to select high-redshift spiral galaxies lensed by a foreground elliptical galaxy from SDSS DR4 spectroscopic sample for HST snapshot follow-up (Koopmans 2004; Bolton 2005). They select red, absorption-dominated spectra –typical for ellipticals– that also display multiple high-redshift emission lines associated with the background lensed spiral galaxy (Bolton et al. 2006; Treu et al. 2006; Koopmans et al. 2006; Gavazzi et al. 2007). It is a straightforward matter to implement the reverse of this algorithm to select absorption-dominated spectra with emission lines at *lower* redshifts, to find spiral disks with a bright background elliptical behind them.

Objects were selected from the fourth data release of the Sloan Digital Sky Survey spectra if they met the following criteria:

1. The redshift is successfully found by the Princeton 1D spectral pipeline (<http://spectro.princeton.edu/>).
2. The objects is classified spectroscopically as a galaxy by this pipeline: the χ^2 fit is better for a galaxy spectrum than a star or QSO.
3. Rest-frame $H\alpha$ equivalent width less than 4 \AA to select ellipticals.
4. Redshift less than 0.4 to enable the $H\alpha$ equivalent width cut in the optical band.
5. At least 3 of 5 lines ($[OII]$, $H\beta$, $[OIII]$, $[OIII]$ and $H\alpha$) are detected at a redshift greater than 0.01 but less than the elliptical’s redshift.

The reversed algorithm yielded 118 candidate occulting pairs in the SDSS DR4 spectral sample. Both galaxies are within the $3''$ aperture of the SDSS fiber, ensuring a small angular

separation of the occulting pair members. In addition, we have visually verified the suitability of each pair and we picked only those that have the ideal pair geometry (Figure 1). The resulting sample is 83 ideal pairs. The Sloan spectroscopy limits us effectively to galaxies with redshifts less than 0.4 ($z < 0.4$), and most of the spirals are closer than 0.3 ($z < 0.3$). Figure 3 shows the distribution of redshifts for the foreground and background galaxies. The majority of the foreground galaxies is nearby ($z < 0.1$) The SDSS DR4 spectral catalog information is listed in Table 1. These spirals, backlit by a bright symmetric elliptical, enable us to measure the extinction to the highest degree of accuracy possible with this technique.

The Sloan Digital Sky Survey (York et al. 2000, SDSS) has mapped one-quarter of the entire sky mainly around the north galactic cap in five bands, u' , g' , r' , i' , z' Smith et al. (2002); Fukugita et al. (1996). SDSS imaging is obtained using a drift-scanning mosaic CCD camera (Gunn et al. 1998) with a pixel size of $0''.396$. We obtained all five bands of the night sky (“corrected frames”) in fits format using the SDSS SkyServer DR5 (<http://cas.sdss.org/dr5/en/tools/ch>). The corrected frames, having been bias subtracted, flat-fielded, and purged of bright stars are stored at SDSS in integer format to save disk space. The pixel values get randomised appropriately before being rounded to make sure that the statistics of the background counts are what they should be. An additional offset (SOFTBIAS) of 1000 counts is added to each pixel to avoid negative pixel values and should be subtracted together with the sky value. We used only single SDSS scans for our analysis (no pair was on the dividing line between scans).

4. Fit to the occulting pair

The uniform approach to the SDSS images of these pairs is to fit the images with the central x and y position of the foreground and background galaxy as free parameters as well as the angle of rotation of both galaxies, 6 free parameters total ($x_{fg}, y_{fg}, \text{pa}_{fg}, x_{bg}, y_{bg}, \text{pa}_{bg}$). The best fit criteria is a minimal residual image, the original image with the two rotated galaxies subtracted. We used a new fit for each SDSS filter. Because the image is used to model itself, we do not need to take the SDSS point spread function into account.

To identify objects in the field and the members of the pair, we ran source extractor v2.5 (Bertin & Arnouts 1996)¹. If both members of the pair are separated and identified in the segmentation by source extractor, we can proceed with the fit. We use the assignments of pixels by source extractor to mask non-pair object. A 100 by 100 pixel postage stamp is cut from the SDSS scan around the pair and used for the further fit with the IDL rou-

¹See also the user manual, Holwerda (2005).

tine *mpfit2dfun*. The mask for each pair member is padded by smoothing it with a 3 pixel wide boxcar. Typical galaxy sizes are several hundred pixels. We use the padded masks to determine which pixels are to be used for the fit. The model subtracted from the original image is the foreground galaxy rotated, plus the background galaxy rotated with the sky value subtracted from the original image. The source extractor catalog used to make the segmentation image also provides the effective radius, ellipticity and flux for both the foreground galaxy and background galaxy. The ellipticity is converted into an inclination estimate ($i = \text{atan}(B/A)$).

We apply two apertures to the extinction map based on the fits, each 5×5 pixels. In the g-band images, we visually identified a good position for an aperture. An additional aperture position can be identified in the extinction map by using the point of maximum extinction as the center of the second aperture. Extinction values for the visual aperture are presented in Tables 2 for the SDSS filters. The disk opacities have been corrected for the inclination ($\times \cos(i)$).

The inclusion of an automatically selected aperture position was to test whether or not this method can be easily automated to apply on large samples of near pairs. It appears that a visual placement of the aperture remains optimal.

The fit fails in case source extractor did not segment the pair into two separate objects or when there is no signal in the visual aperture. Negative extinction values occur when the galaxies are significantly asymmetric but the fit does not explicitly fail. We include these negative opacity values because it gives an indication of the dominant remaining uncertainty in these measurements.

Figure 4 shows the redshift distributions for pairs with a successful fit. An opacity measurement of a spiral disk from SDSS images is feasible for disks closer than $z=0.2$. The fit fails for more distant disks as the pair cannot be resolved into separate objects.

5. Results

The optical depth value of a spiral disks depends a great many factors, radius, arm presence, Hubble type and possibly disk luminosity. In this section we explore some relations between disk opacities and other disk characteristics, radius, disk luminosity and surface brightness. Finally, we present radial plots based on stacked SDSS filters together to improve signal-to-noise.

5.1. Radial profiles

Figure 6 shows the radial profiles based on the visual apertures for all five SDSS filters (g' , r' , i' , u' , z') and split up into three redshift ranges ($z < 0.05$, $0.05 < z < 0.1$ and $z > 0.1$). Figure 7 shows the same plot for the automated aperture. The increase of scatter in the automatic aperture does indicate that the visual aperture is better placed to measure disk opacity. The opacity values have been corrected for inclination ($\times \cos(i)$). The r' and i' filter has the best extinction signal. Notably, the u' band fits are all failures as the early type background galaxy is too faint in this band and the foreground galaxy possibly too irregular. The reason that the most extinction signal is in the r' and i' filters is because these are blue enough to exhibit strong dust extinction but red enough to benefit from a symmetric distribution of the light in both galaxies. Bluer filters are more asymmetric due to localized star formation in the foreground galaxy's spiral arms. This is in agreement with HST/WFPC2 results in local galaxies (Keel & White 2001a,b).

The resolution of the SDSS for these pairs is unfortunately not sufficient to distinguish between arm and disk sections similar to previous studies in the very local universe. In order to obtain similar quality measurements, one would greater resolving power such as HST. The opacity values in Figure 6 are therefore a mix between the arm and disk values.

Similarly, distinguishing Hubble subtypes for these galaxies is equally impossible and hence the opacities represent also mix between earlier and later type spiral, which most likely have different opacities (White et al. 2000; Holwerda et al. 2005a).

Because of the many other influences and the small span of the redshift range in Figure 6 it is impossible to conclude if there is any evolution in the opacity of spiral disks from the single-filter SDSS data. However, we can conclude that optical disks show evidence of extinction up to twice their effective radius in all SDSS filters except u , which is due to low S/N from the red background galaxy.

5.2. Exponential fits

In both Figures 6 and 7 we show the least-square fit of an exponential disk to the positive points (fit-parameters are listed in Table 5 and 4). The fits are poor and unrealistic (increasing with radius) for many of the SDSS filters. For a better fit, one would need better S/N and distinguish between arm and disk sections .

5.3. Disk opacity and luminosity

Tully et al. (1998) and Masters et al. (2003) note a relation between disk opacity and overall luminosity. A similar relation for sections of the disks between surface brightness and opacity in spiral arms is noted in Holwerda et al. (2005a,b). Figure 8 shows the relations between magnitude of the foreground galaxy and disk opacity for all the SDSS filters. No relation can be seen. Figure 9 is the relation between optical depth and surface brightness in the visual aperture. In nearby galaxies there is appears to be a relation between the two (Holwerda et al. 2005b), but there is little evidence that brighter disks are also more opaque here.

5.4. Extinction law

With several independent disk opacity measurements in four different filters, one could construct a reddening law for disks at higher redshift. However, the optical depths in the visually identified aperture agree with each other in all four filters (See Figure 6). As noted by Keel & White (2001a), disk opacity is effectively gray unless sampled over disk sections smaller than 100 pc. The explanation is that the ISM is very clumpy, resulting in a gray extinction law when averaged over larger sections.

5.5. Stacked images

In order to improve the S/N of our measurement and given the expected lack of an extinction law, we have stacked various combinations of the SDSS filter images and fit them as a single SDSS filter field. In Table 3 and Figure 11, the results are summarized. The noise does appear somewhat reduced in the radial profiles using r+i stacked fields (Figure 11). Stacking more fields together or a different combination did not result in any improvement of S/N (Table 3).

We note that the optical depth measurements in our sample are at similar radii as those by White et al. (2000); Domingue et al. (2000) (see Figure 11). As in Figures 6 and 7, we fit an exponential profile to the points (parameters in Table 6), both to the Domingue et al. (2000) points and the r+i opacity points at different redshift. The higher redshift profile fits are extremely flat, with high scale-lengths. If we compare the higher redshift profiles to the nearby points, they resemble the arm profile more than the disk. However, much of the profile is determined by opacity measurements nearer to the center of the spiral galaxy.

We do not have meaningful extinction measurements close to the center of the foreground spiral as there is not enough flux from the background galaxy. In a deeper image, there would be significant flux from the background elliptical nearer to the center of the spiral, enough to make a significant extinction measure there. The pairs did get selected however because both fell within the 3" of the SDSS spectroscopic aperture. Together with the resolution to distinguish between arm and disk, this is another argument for follow-up with HST or possibly a large ground-based telescope.

6. Discussion and conclusions

The occulting galaxy technique is a well established one to measure disk extinction in the local universe. In combination with the wealth of data in the SDSS, we can construct a recent history of average disk extinction since $z \sim 0.3$. However, due to the spatial resolution, this disk opacity history is for the mix or arm and disk regions for all late-type disks. The redder optical bands have proven themselves to be optimal for opacity measurements in these pairs due to the brightness of the background early type and less asymmetry in the foreground spiral.

From our analysis of 83 occulting pairs in the SDSS DR4 we can conclude the following:

1. Selection of occulting galaxy pairs from a uniform spectroscopic sample like the SDSS has a very high rate of success resulting in a substantial sample (§3).
2. Fits to occulting pairs can be automated yet the optimal placement of an aperture to measure the disk opacity can not (§2, Figure 6 and 7).
2. The i' and r' filters in SDSS are optimal for measuring disk opacity in more distant galaxy pairs (Figure 6).
3. The radial plots are similar to those found by White et al. (2000) for a mix of arm and disk values (Figure 11).
4. There is not enough redshift range in the current sample with successful fits to distinguish an evolutionary trend in disk opacity (Figure 11).
5. There is no relation between overall disk luminosity and local disk opacity and only a weak relation between local surface brightness and disk opacity, probably because arms cannot be resolved at these distances by SDSS (Figures 8 and 9).

6. Optical depth values in different filters agree with scatter due to the different asymmetry in galaxies in different filters, consistent with earlier findings (Figure 10).
7. Stacking SDSS images does result in some S/N improvements. In order to probe the inner parts of the spirals, deeper exposures are needed (Figure 11).
8. The exponential profile of disk opacity for the higher redshift pairs is flatter than that of the nearby ones from Domingue et al. (2000). More points at lower galactic radius are needed to confirm (Figure 11).

7. Future Work

These SDSS pairs constitute the ideal sample for study of spiral disks opacity in the local Universe ($z < 0.4$). For these and more distant pairs, the photometric stability and high resolution of HST will be needed to 1) resolve Hubble sub-type, 2) distinguish between arm and disk sections and allow for optical depth values closer to the center of the spiral. The SDSS measurements can however serve as a reference for higher-redshift pairs images with HST for which Hubble type and spiral arm identification also remain impossible.

The authors would like to thank Roelof de Jong, Ron Allen, and Harry Ferguson for useful discussions. We thank Lorraine and Steve Mencinsky for assistance in examining each candidate pair for suitable geometry. Funding for the Sloan Digital Sky Survey (SDSS) has been provided by the Alfred P. Sloan Foundation, the Participating Institutions, the National Aeronautics and Space Administration, the National Science Foundation, the U.S. Department of Energy, the Japanese Monbukagakusho, and the Max Planck Society. The SDSS Web site is <http://www.sdss.org/>.

The SDSS is managed by the Astrophysical Research Consortium (ARC) for the Participating Institutions. The Participating Institutions are The University of Chicago, Fermilab, the Institute for Advanced Study, the Japan Participation Group, The Johns Hopkins University, Los Alamos National Laboratory, the Max-Planck-Institute for Astronomy (MPIA), the Max-Planck-Institute for Astrophysics (MPA), New Mexico State University, University of Pittsburgh, Princeton University, the United States Naval Observatory, and the University of Washington. W. C. Keel is grateful for support from a Dean's Leadership Board Faculty Fellowship.

REFERENCES

- Andredakis, Y. C., & van der Kruit, P. C. 1992, *A&A*, 265, 396
- Berlind, A. A. et al. 1997, *AJ*, 114, 107
- Bertin, E., & Arnouts, S. 1996, *A&AS*, 117, 393, provided by the NASA Astrophysics Data System
- Bolton, A. 2005, in *HST Proposal*, 6907–+
- Bolton, A. S. et al. 2006, *ApJ*, 638, 703
- . 2004, *AJ*, 127, 1860
- Calzetti, D., & Heckman, T. M. 1999, *ApJ*, 519, 27
- Domingue, D. L. et al. 1999, *AJ*, 118, 1542
- . 2000, *ApJ*, 545, 171
- Elíasdóttir, Á. et al. 2006, *ApJS*, 166, 443
- Elmegreen, D. M. et al. 2001, *AJ*, 121, 182
- Falco, E. E. et al. 1999, *ApJ*, 523, 617
- Fukugita, M. et al. 1996, *AJ*, 111, 1748
- Gavazzi, R. et al. 2007, *astro-ph/0701589*
- Gunn, J. E. et al. 1998, *AJ*, 116, 3040
- Holwerda, B. W. 2005, *astro-ph/0512139*
- Holwerda, B. W. et al. 2005a, *AJ*, 129, 1396
- . 2005b, *A&A*, 444, 109
- Hopkins, P. F. et al. 2004, *AJ*, 128, 1112
- Jha, S. et al. 2007, *ApJ*, 659, 122
- Keel, W. C., & White, R. E. 2001a, *AJ*, 121, 1442
- . 2001b, *AJ*, 122, 1369

- Knop, R. A. et al. 2003, ApJ, 598, 102
- Koopmans, L. 2004, in HST Proposal, 6492–+
- Koopmans, L. V. E. et al. 2006, ApJ, 649, 599
- Masters, K. L. et al. 2003, AJ, 126, 158
- Motta, V. et al. 2002, ApJ, 574, 719
- Nadeau, D. et al. 1991, ApJ, 376, 430
- Nilsson, K. K. et al. 2007, astro-ph/0706.1070
- Rowan-Robinson, M. 2003, MNRAS, 344, 13
- Rowan-Robinson, M. et al. 2005, AJ, 129, 1183
- Sajina, A. et al. 2006, MNRAS, 369, 939
- Smith, J. A. et al. 2002, AJ, 123, 2121
- Treu, T. et al. 2006, ApJ, 640, 662
- Tully, R. B. et al. 1998, AJ, 115, 2264
- Vijh, U. P. et al. 2003, ApJ, 587, 533
- Warren, S. J. et al. 1996, MNRAS, 278, 139
- White, R. E., & Keel, W. C. 1992, Nature, 359, 129
- White, R. E. et al. 2000, ApJ, 542, 761
- Yan, H. et al. 2005, ApJ, 634, 109
- York, D. G. et al. 2000, AJ, 120, 1579

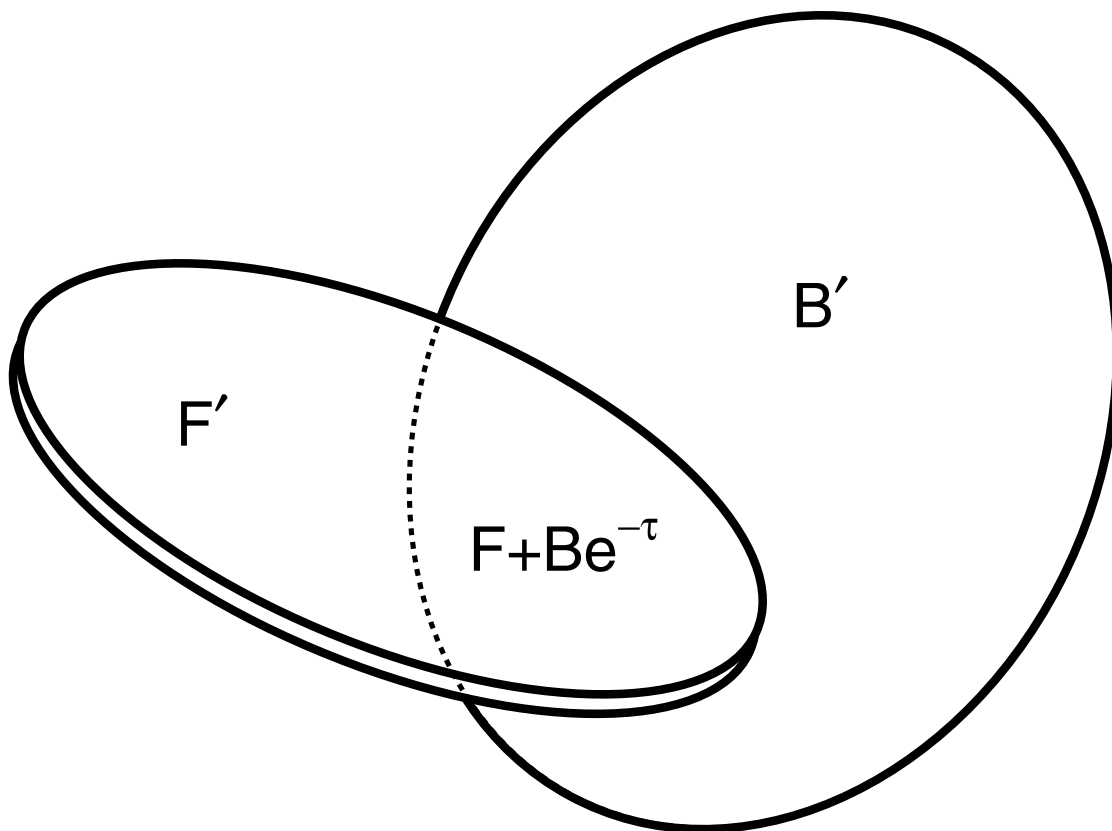


Fig. 1.— A schematic of the ideal occulting pair. The background galaxy is a symmetric elliptical galaxy and the foreground galaxy a symmetric spiral. In the overlap region, the elliptical is bright enough to provide an extinction signal but the elliptical is not completely hidden behind the spiral so the contribution of the elliptical to the overlap region can be estimated from the non-occulted part.

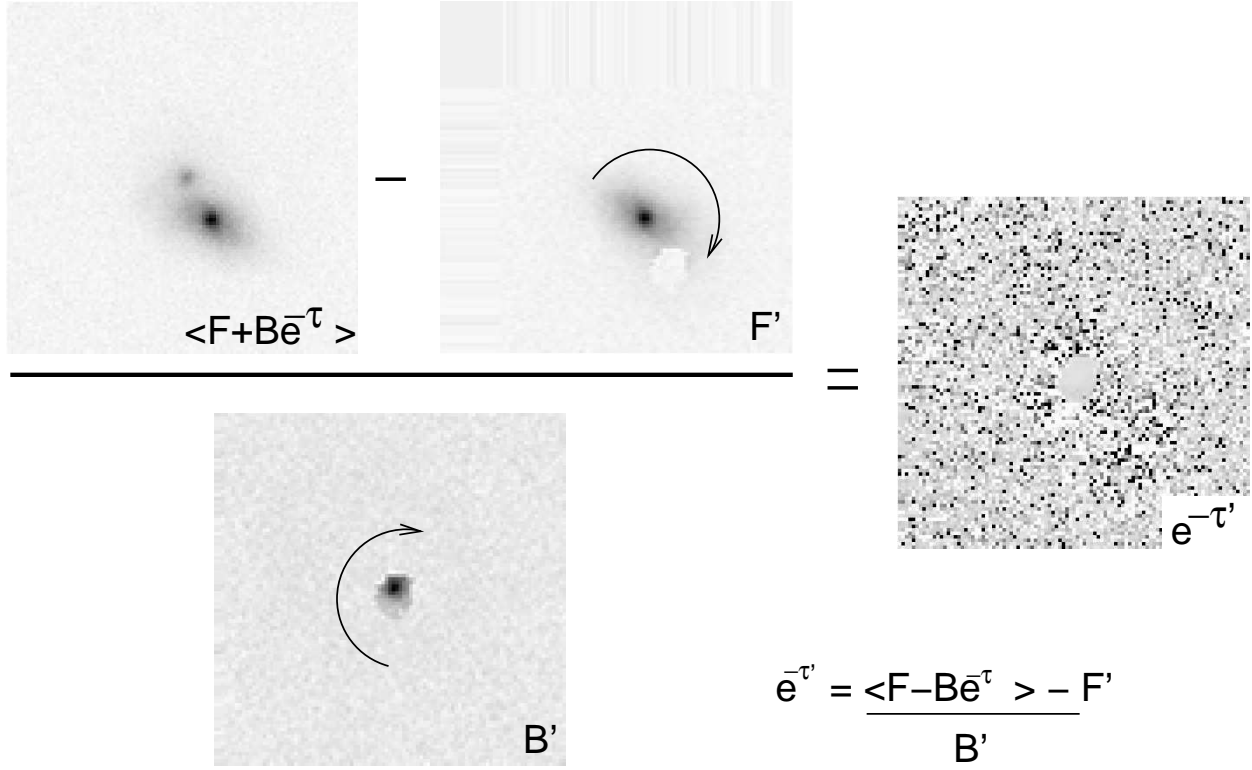


Fig. 2.— A schematic of the automated occulting galaxy method with the pair 1006-52708-624. The extinction map is constructed when the fit parameters (central positions and rotation angles) of both pair members have been determined. The foreground galaxy is rotated and subtracted with the resulting image divided by the flipped background image. The resulting image is the opacity map. In case the area of the background image is perfectly unity, both galaxies are perfectly symmetric and there is no extinction.

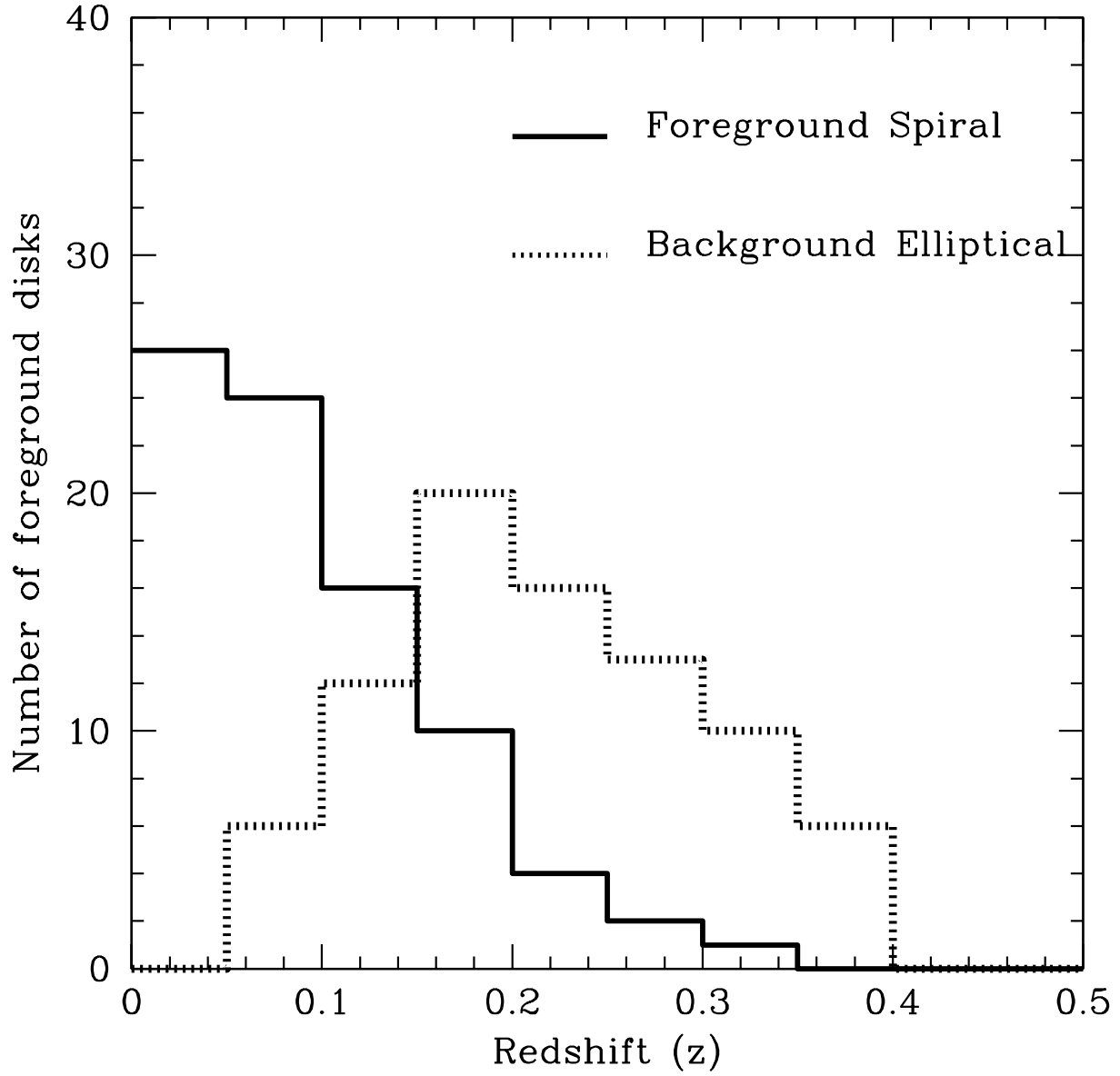


Fig. 3.— The histogram of redshift distribution of both the background and foreground galaxy. The majority of pairs is nearby ($z < 0.1$). The spectroscopic selection from the SDSS limits the pairs to closer than $z = 0.4$.

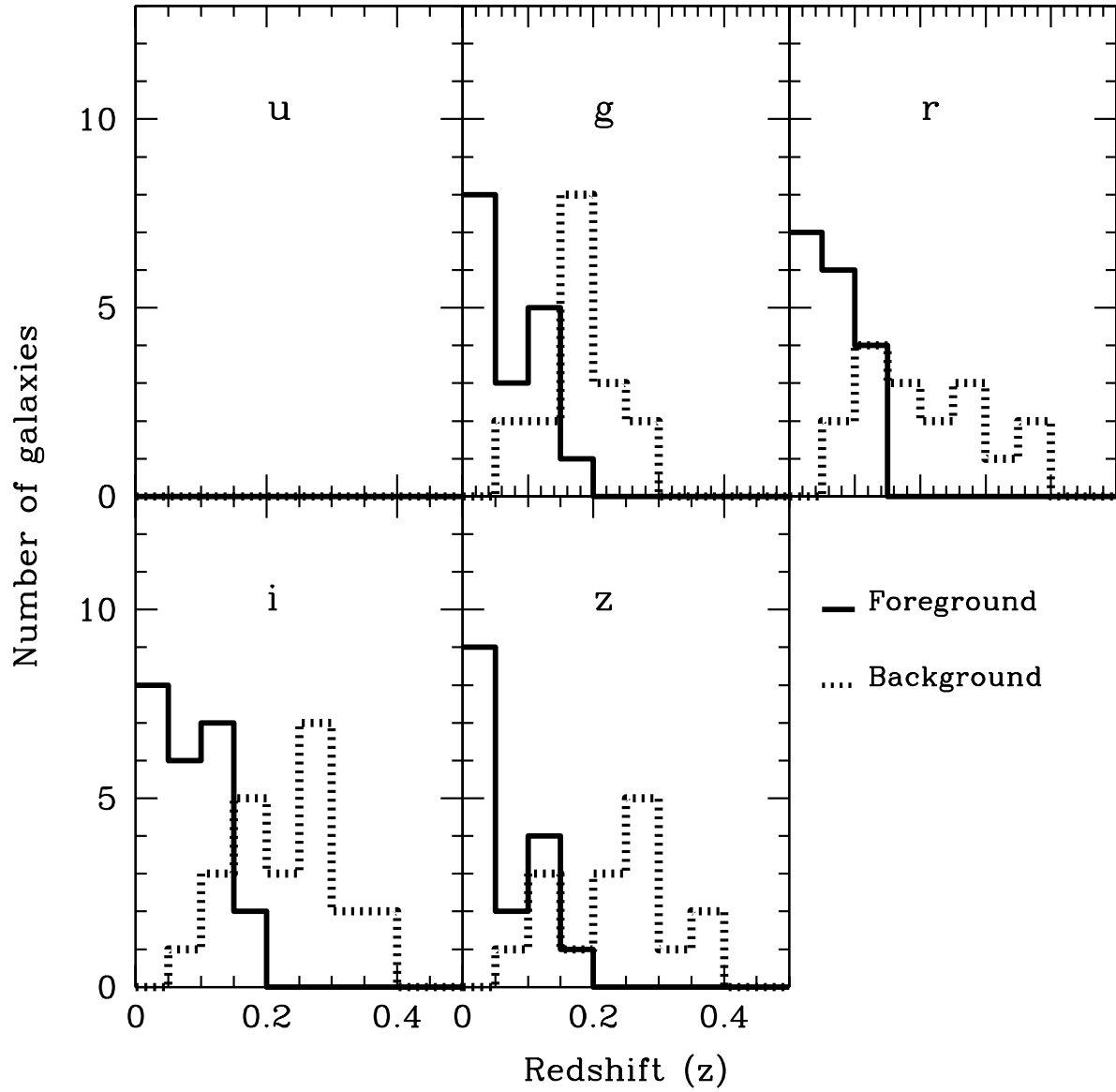


Fig. 4.— The histogram of redshift distribution of both the background and foreground galaxies in pairs for which a successful fit is found. No good fits are obtained for the u band and only disks closer than $z=0.2$ could be fitted.

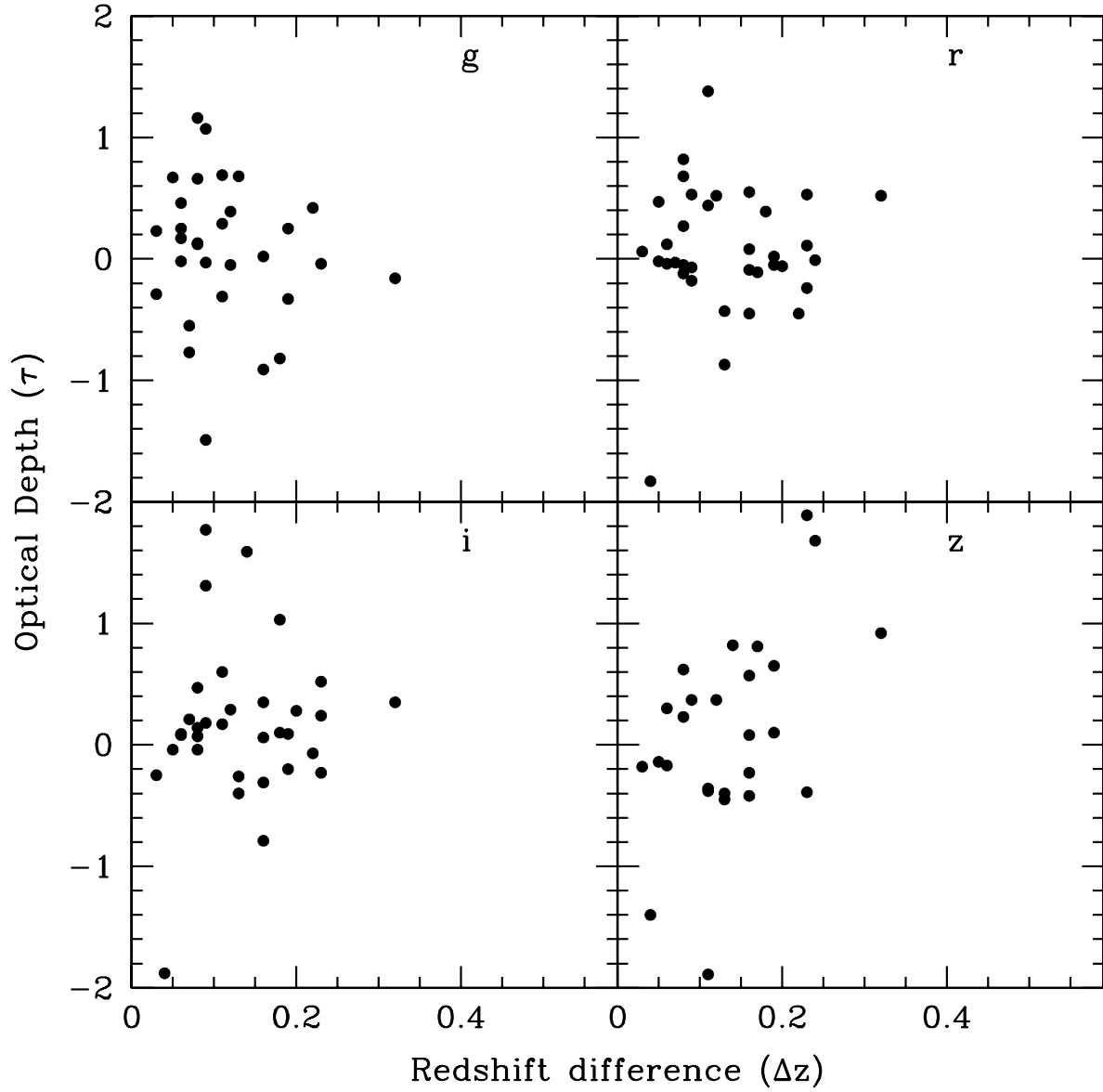


Fig. 5.— The plots of the redshift distance between foreground and background galaxy and the derived optical depth in the visual aperture in the SDSS for which meaningful opacities can be obtained. There appears to be no systematic relation between the distance between the pair members and the optical depth inferred.

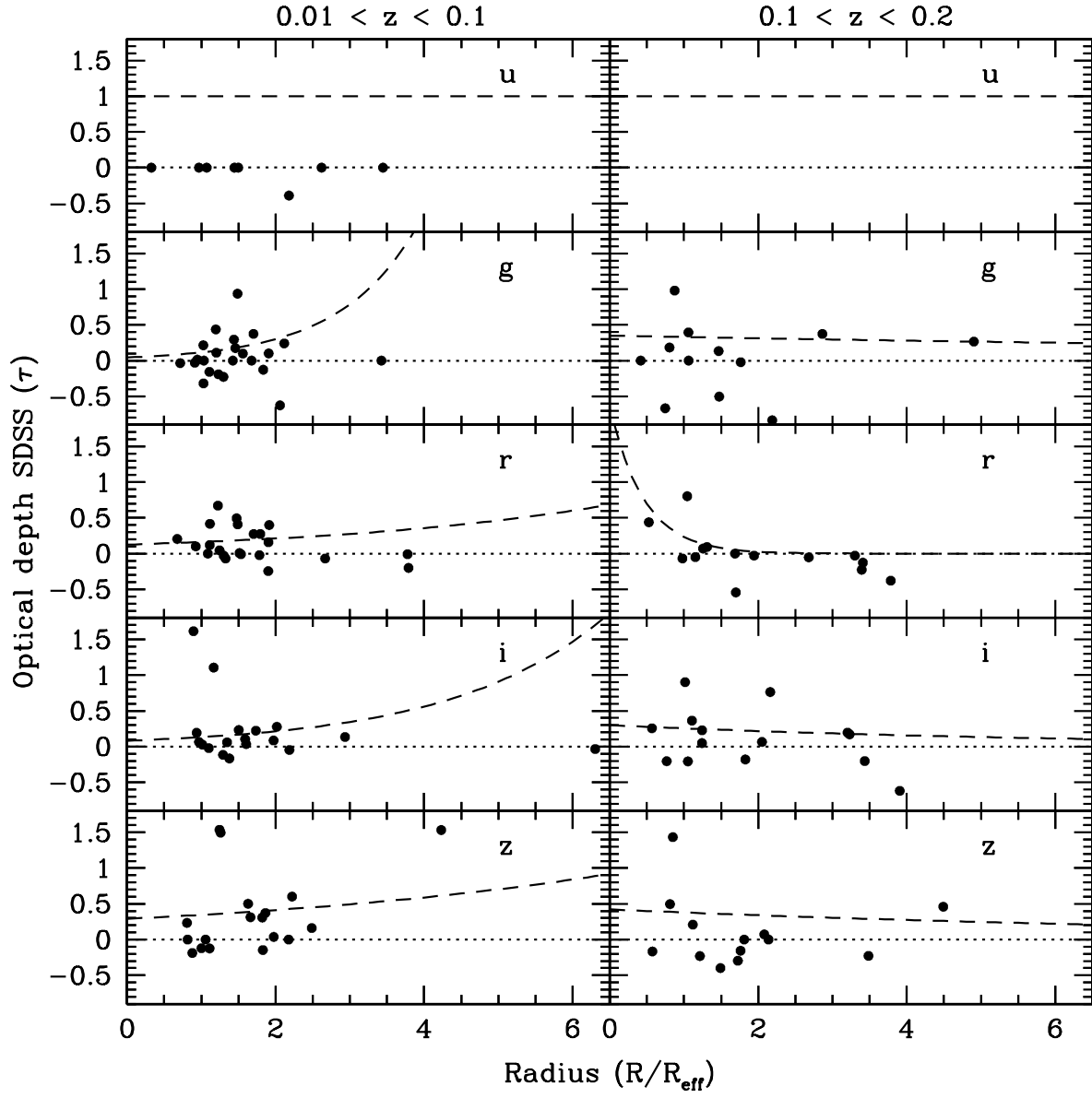


Fig. 6.— Disk opacity in the visual aperture as a function of radius in all five SDSS filters; **top:** $z < 0.05$, **middle:** $0.05 > z > 0.1$, **bottom:** $z > 0.1$. The dashed lines represent an exponential fit to the positive optically thin opacity values.

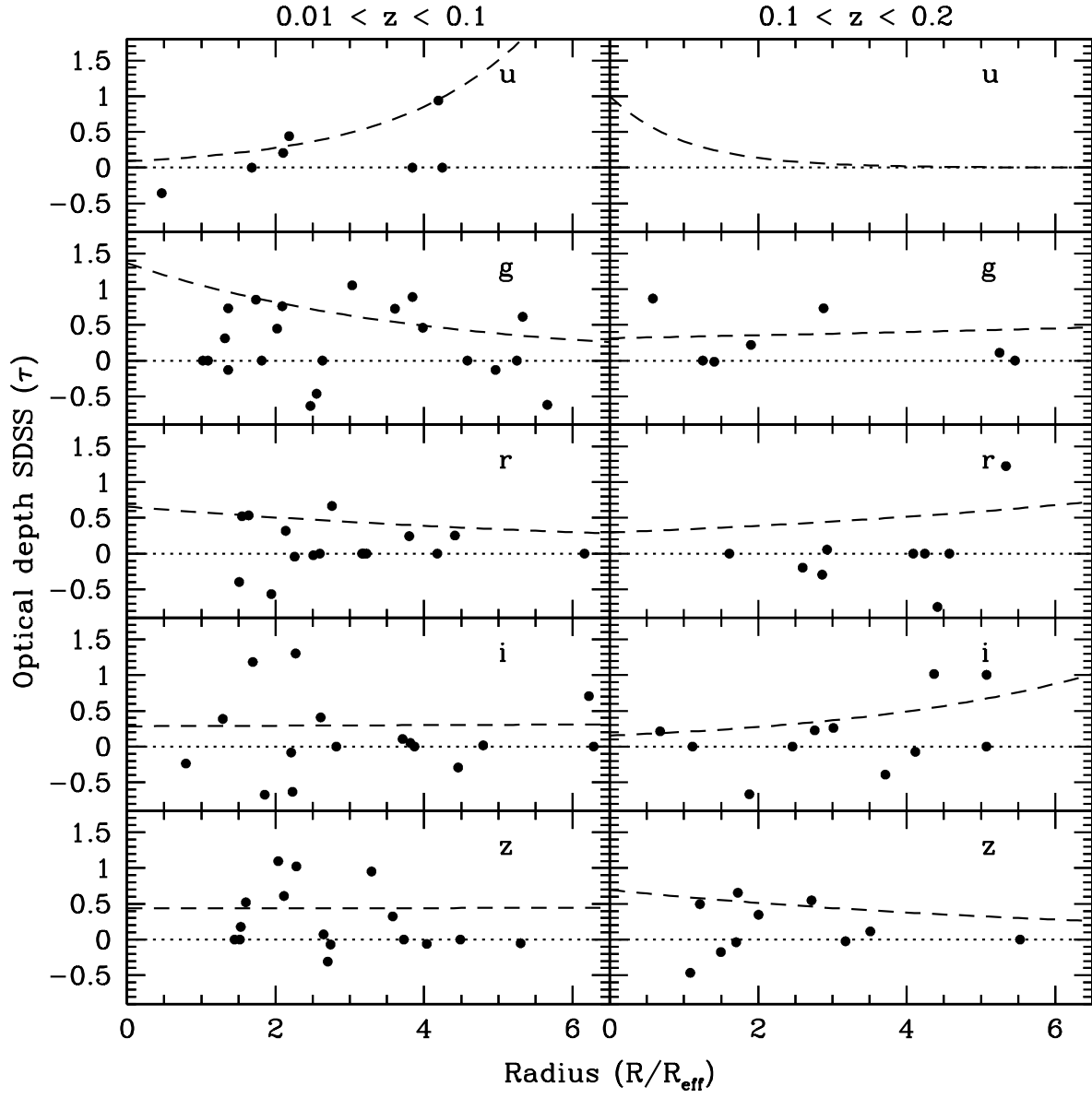


Fig. 7.— Disk opacity in the automatic aperture as a function of radius in all five SDSS filters; **top**: $z < 0.05$, **middle**: $0.05 > z > 0.1$, **bottom**: $z > 0.1$. The dashed lines represent an exponential fit to the positive optically thin opacity values.

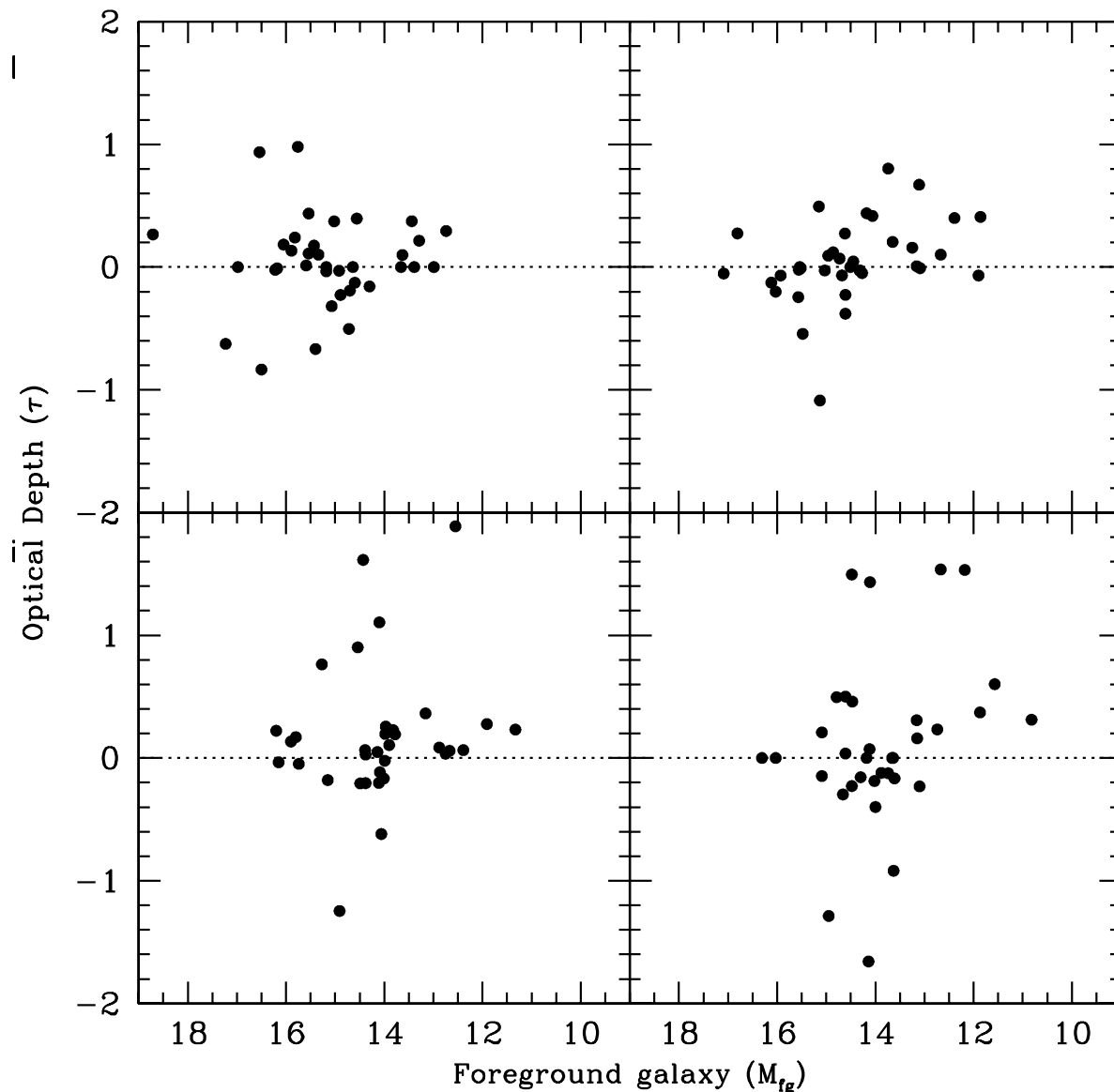


Fig. 8.— The plot of disk optical depth and foreground galaxy magnitude –measured by the source extractor run part of the fit. There appears to be little relation between optical depth and disk brightness, probably because other affects –radial distance, arm presence and Hubble type– dominate the optical depth value. Negative optical depth values occur when there is significant asymmetry in either or both of the members of the occulting pair.

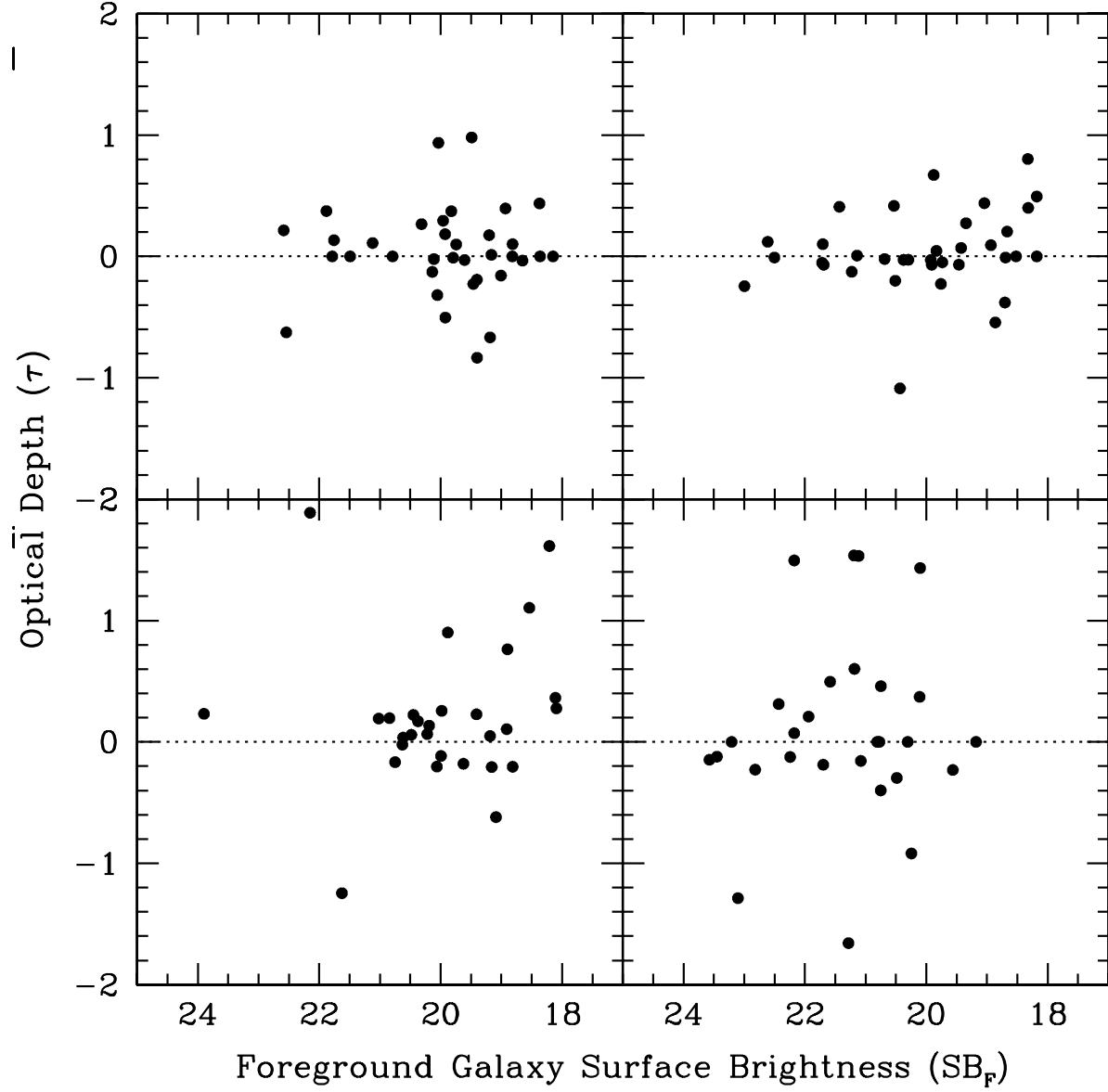


Fig. 9.— The plot of disk optical depth and foreground galaxy surface brightness in the aperture. No relation is evident.

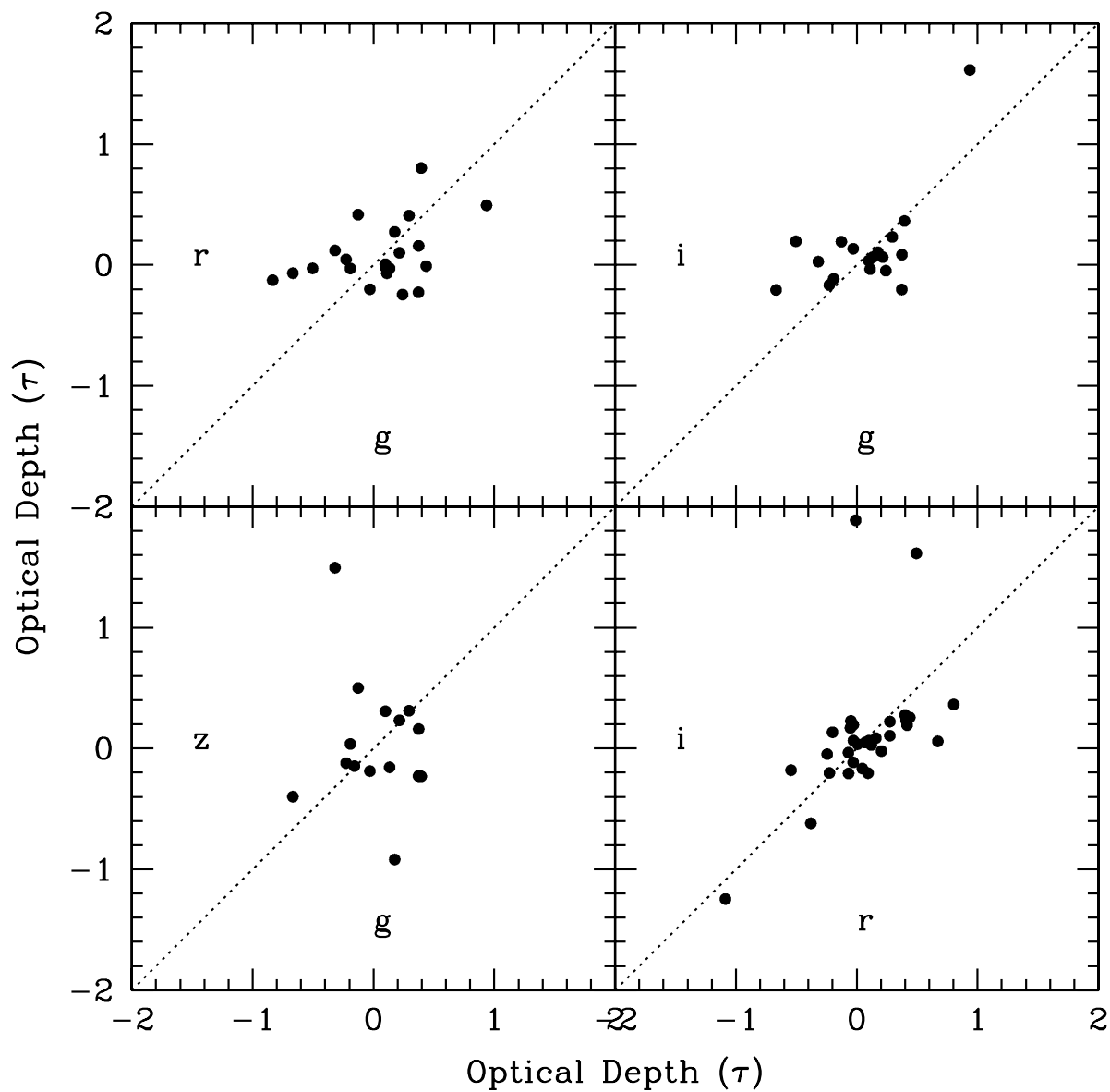


Fig. 10.— The relation between opacity measurements in the visual aperture for four different SDSS filters (g' , r' , i' , z'). Only the non-zero opacities are shown. The values agree for the most part for the visual aperture as a Galactic extinction law is expected to be resolved only when the spatial scale is less than 100 pc.

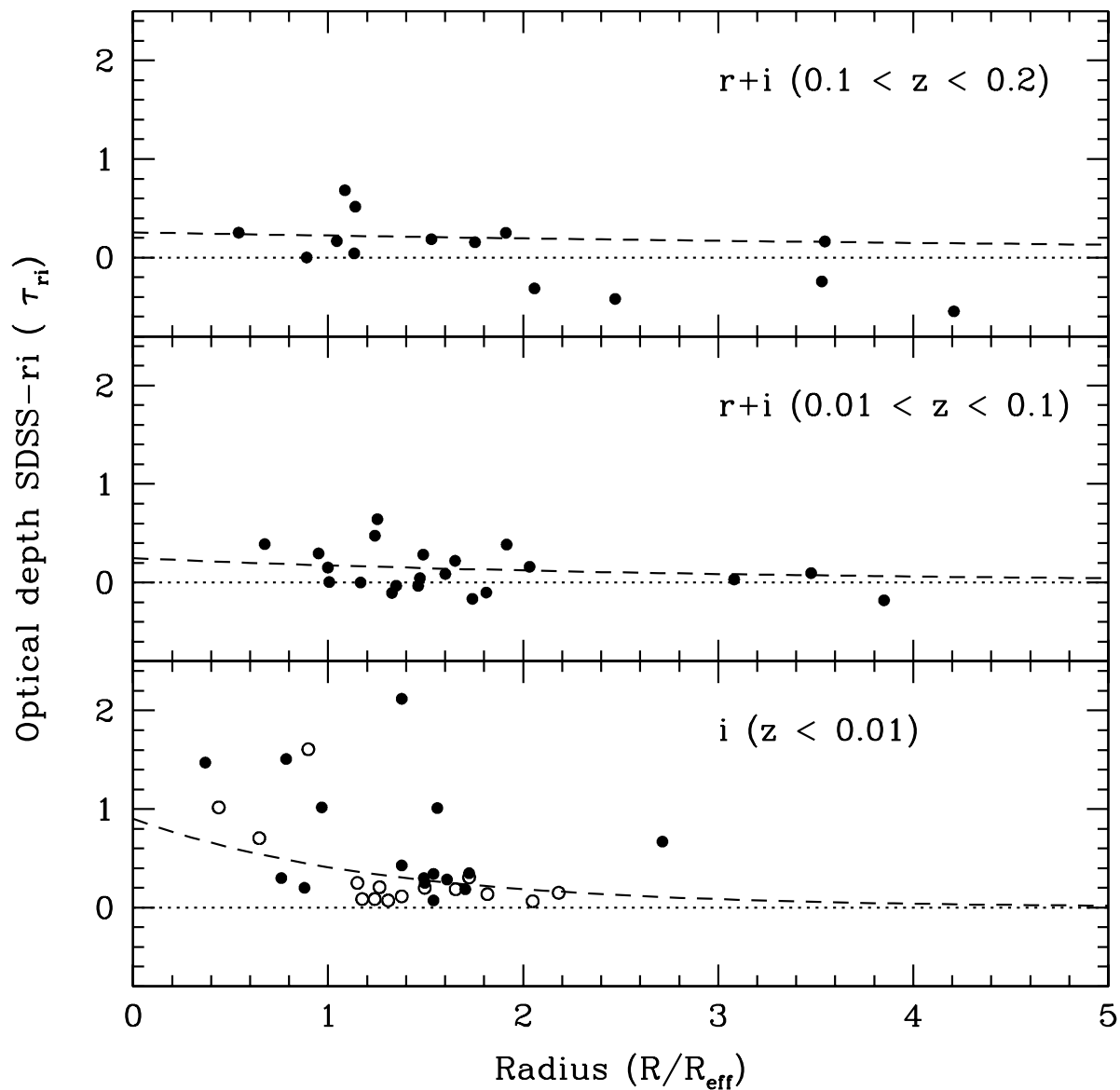


Fig. 11.— The radial profile from Figure 14 in Domingue et al. (2000) (lower panel) and the optical depths profile from the r+i stacked image. The R_{25} from Domingue et al. (2000) was converted to effective radius with $R_{25} = 1.43 \times R_{eff}$. Open circles are for disk regions, filled for spiral arm in the case of the Domingue et al. (2000) values. Exponential disk fits to the points are the dashed lines.

Table 1. The SDSS basic data of the occulting galaxy pairs.

plate	mjd	fiber	ra	dec	zfg	zbg	u	g	r	i	z
267	51608	499	148.311890	0.649980	0.0355	0.0941	22.79	20.11	18.79	18.20	17.66
273	51957	323	156.808510	0.680520	0.1071	0.1781	21.23	19.62	18.54	18.01	17.63
275	51910	233	161.287840	0.075950	0.0260	0.0944	21.22	19.10	18.07	17.54	17.24
281	51614	624	173.070050	0.608420	0.0468	0.1988	22.20	20.20	19.01	18.51	18.04
282	51658	120	174.666790	-0.146470	0.0722	0.2600	23.92	21.60	19.94	19.15	18.53
285	51930	15	180.269580	-0.787540	0.0213	0.1408	21.55	20.38	19.70	20.27	19.81
313	51673	546	231.835980	0.477040	0.0413	0.3033	23.41	21.07	19.43	18.85	18.42
367	51997	222	259.541780	55.201470	0.0836	0.1394	21.30	19.50	18.44	17.94	17.54
403	51871	586	30.145580	0.560980	0.1378	0.1658	21.70	19.71	18.58	18.04	17.66
408	51821	336	38.992950	1.257390	0.0682	0.1243	23.31	20.47	19.34	18.65	18.23
435	51882	118	118.882910	40.503790	0.2313	0.2620	23.54	21.07	19.45	18.82	18.32
436	51883	638	120.747080	45.492670	0.0389	0.3643	23.75	22.78	20.48	19.75	19.28
440	51885	370	123.106550	50.404870	0.1756	0.2453	23.91	21.72	20.09	19.24	18.93
464	51908	211	58.942650	-5.948270	0.1230	0.2011	24.24	20.67	19.37	18.68	18.22
474	52000	548	142.017490	0.242640	0.2061	0.2970	22.94	20.72	19.15	18.58	18.21
484	51907	616	139.814360	59.294570	0.1582	0.2453	25.28	21.65	19.81	19.15	18.83
487	51943	305	147.228910	62.483730	0.1245	0.2479	24.03	21.38	19.78	19.09	18.70
497	51989	73	208.034660	65.742370	0.1953	0.3958	23.67	21.82	20.06	19.23	18.63
499	51988	152	217.024030	63.613230	0.1145	0.2863	25.86	22.30	20.05	19.48	19.10
511	52636	313	169.186260	2.065220	0.1292	0.2673	22.10	20.43	19.16	18.52	18.12
512	51992	302	171.158050	1.820180	0.0492	0.2321	22.85	20.44	18.90	18.32	17.94
529	52025	408	205.440810	3.431220	0.0232	0.1681	21.74	19.97	18.92	18.45	18.14
545	52202	504	121.639780	40.920020	0.0764	0.3170	24.52	22.43	20.28	19.58	19.19
547	52207	167	124.385840	43.503210	0.1415	0.3761	24.73	22.51	20.37	19.56	19.05
550	51959	624	131.782940	48.626320	0.1743	0.1975	24.74	21.65	19.57	18.89	18.57
628	52083	262	249.181810	41.790430	0.0284	0.1203	21.19	19.49	18.55	18.18	17.75
629	52051	26	252.894690	43.849070	0.1152	0.3502	23.01	22.07	20.40	19.41	19.08
637	52174	334	314.058170	-6.743460	0.0878	0.1779	23.42	20.95	19.29	18.65	18.31
671	52206	347	34.784680	0.615480	0.0408	0.2803	22.02	21.57	20.60	20.28	19.76
765	52254	179	137.082920	49.082730	0.0355	0.2128	21.32	19.83	18.68	18.18	17.80
782	52320	306	190.878970	62.349390	0.1452	0.2056	22.21	20.15	18.82	18.25	17.87
790	52441	527	219.458290	58.911160	0.0317	0.1381	22.33	19.79	18.59	18.08	17.81
792	52353	432	224.462030	56.091590	0.1423	0.2012	22.25	20.27	18.77	18.19	17.85
808	52556	39	46.965700	-0.311940	0.2139	0.3731	23.21	21.72	20.34	19.66	19.27
845	52381	270	187.675090	4.707290	0.0700	0.3164	24.73	21.85	19.52	18.88	18.60
848	52669	602	195.053830	5.739970	0.0490	0.2219	22.22	20.39	19.20	18.80	18.39
860	52319	451	121.339030	30.762010	0.0370	0.1607	21.94	21.15	18.59	17.94	17.59

Table 1—Continued

plate	mjd	fiber	ra	dec	zfg	zbg	u	g	r	i	z
864	52320	91	129.972990	35.742270	0.0439	0.2576	22.17	20.78	19.72	19.18	18.83
877	52353	458	166.000290	51.786350	0.0370	0.0616	21.28	20.11	19.54	19.19	19.01
882	52370	122	180.578770	51.309050	0.0599	0.1828	21.51	19.41	18.26	17.76	17.45
883	52430	366	182.350150	53.640160	0.0492	0.1319	21.68	19.73	18.65	18.12	17.73
884	52374	242	186.059060	51.293770	0.0413	0.1745	21.35	19.56	18.42	17.94	17.62
889	52663	408	116.692660	30.657980	0.0558	0.1612	21.44	19.77	18.57	18.02	17.63
896	52592	463	131.060470	43.308520	0.0275	0.1059	21.57	19.52	18.41	17.96	17.56
913	52433	151	206.813230	-2.646100	0.0843	0.1583	21.77	19.58	18.32	17.79	17.38
931	52619	84	124.763000	29.720850	0.1835	0.2781	22.60	20.79	19.32	18.68	18.28
958	52410	194	197.246590	59.181390	0.1523	0.3145	25.22	21.71	20.00	19.28	19.05
970	52413	408	183.318710	51.174320	0.3046	0.3819	22.92	21.27	19.78	19.08	18.60
973	52426	519	255.808640	33.511540	0.0631	0.0914	21.88	19.07	18.00	17.47	17.15
977	52410	539	258.531050	29.864680	0.0824	0.1954	22.13	19.91	18.67	18.11	17.80
980	52431	300	258.937370	27.421190	0.1253	0.2907	24.22	21.76	19.48	18.78	18.44
1000	52643	337	159.372270	7.579740	0.0851	0.3245	24.23	21.53	19.44	18.83	18.51
1006	52708	624	152.436350	49.838300	0.0524	0.1323	21.96	19.99	18.47	18.02	17.50
1007	52706	519	153.131040	50.738660	0.0463	0.1952	21.60	19.74	18.47	17.93	17.63
1160	52674	468	214.447800	56.804440	0.2381	0.2914	22.28	20.80	19.58	19.12	18.81
1215	52725	288	143.281310	39.220680	0.2708	0.3340	22.71	21.18	19.56	18.95	18.60
1230	52672	639	185.753290	10.099700	0.0536	0.1608	21.67	20.04	19.04	18.57	18.17
1235	52734	164	148.326780	7.600730	0.0956	0.3255	22.21	20.84	19.34	18.73	18.33
1269	52937	485	130.654940	30.422070	0.0272	0.1878	21.30	19.90	18.91	18.48	18.23
1280	52738	125	195.231990	48.583740	0.0799	0.2089	21.89	20.13	18.95	18.45	18.14
1282	52759	630	202.872560	49.243360	0.1245	0.2786	21.92	20.42	19.06	18.51	18.14
1310	53033	202	173.008190	56.231840	0.1140	0.1840	21.76	19.95	18.75	18.26	17.89
1317	52765	9	192.781290	56.429170	0.0974	0.2008	21.59	19.86	18.60	18.06	17.64
1321	52764	461	203.989570	56.632780	0.1528	0.2173	22.30	20.49	19.11	18.56	18.24
1324	53088	50	212.489360	53.497750	0.0422	0.2251	22.31	20.52	19.31	18.79	18.46
1325	52762	313	211.388780	54.126820	0.1168	0.2119	22.14	20.29	18.96	18.48	18.10
1327	52781	252	218.738380	51.467310	0.0799	0.1408	21.41	19.79	18.77	18.31	17.97
1332	52781	469	233.667240	46.404020	0.2849	0.3199	22.41	20.89	19.44	18.89	18.57
1363	53053	104	166.400210	42.239340	0.1759	0.2673	22.44	20.71	19.28	18.73	18.41
1373	53063	255	191.929650	43.917920	0.0294	0.1317	21.48	19.63	18.61	18.20	17.87
1388	53119	618	233.838020	32.213560	0.0370	0.2180	21.91	20.30	19.18	18.69	18.36
1390	53142	385	236.455400	29.691260	0.1313	0.2863	22.17	20.44	19.02	18.42	18.02
1402	52872	554	236.160490	35.176090	0.0550	0.0790	21.02	19.26	18.35	17.90	17.60
1416	52875	490	236.353870	36.378000	0.0653	0.1909	21.48	20.05	19.03	18.56	18.17

Table 1—Continued

plate	mjd	fiber	ra	dec	zfg	zbg	u	g	r	i	z
1423	53167	528	250.832630	26.703910	0.1975	0.3322	22.71	21.35	19.89	19.30	18.92
1426	52993	385	151.191870	37.772590	0.0232	0.0519	20.39	18.62	17.78	17.40	17.09
1429	52990	336	156.275830	45.059290	0.0742	0.1461	21.44	19.68	18.50	17.97	17.62
1604	53078	459	168.059410	12.811400	0.0771	0.1681	21.30	19.22	18.03	17.54	17.15
1607	53083	48	174.721650	11.288210	0.0814	0.1513	21.59	19.93	18.80	18.42	18.00
1618	53116	285	171.000090	6.105510	0.0370	0.1741	21.50	19.68	18.56	18.11	17.74
1620	53137	175	175.693770	7.235100	0.0653	0.1011	21.21	19.36	18.38	17.89	17.50
1677	53148	262	226.092130	43.630090	0.1931	0.3080	22.36	20.87	19.45	18.88	18.46
1746	53062	533	155.484860	14.117880	0.1402	0.2469	22.03	20.37	19.02	18.46	18.12

Table 2. The optical depths of the SDSS filters. These values have not been corrected for inclination.

plate	mjd	fiber	z_{fg}	z_{bg}	R	Incl	τ_u	τ_g	τ_r	τ_i
267	51608	499	0.04	0.09	...	0.0	...	0.44 (3.65)	-0.01 (26.35)	...
273	51957	323	0.11	0.18	...	0.0
275	51910	233	0.03	0.09	0.81 (0.13)	39.0	-0.39 (2.39)	0.21 (3.61)	0.10 (11.02)	0.06 (2.14)
281	51614	624	0.05	0.20	...	0.0
282	51658	120	0.07	0.26	1.82 (0.27)	61.7	...	0.10 (2.19)	0.01 (3.85)	0.04 (5.93)
285	51930	15	0.02	0.14	...	0.0
313	51673	546	0.04	0.30	...	0.0	...	-4.76 (1.94)
367	51997	222	0.08	0.14	...	0.0
403	51871	586	0.14	0.17	...	0.0
408	51821	336	0.07	0.12	1.11 (0.45)	27.7	0.20 (4.11)	-0.02 (1.86)
435	51882	118	0.23	0.26	...	0.0
436	51883	638	0.04	0.36	1.63 (0.27)	57.0	...	-0.13 (4.92)	0.42 (2.31)	0.19 (1.88)
440	51885	370	0.18	0.25	...	0.0
464	51908	211	0.12	0.20	...	0.0	...	0.98 (3.12)
474	52000	548	0.21	0.30	...	0.0
484	51907	616	0.16	0.25	...	0.0	...	-0.83 (6.27)	-0.13 (2.13)	...
487	51943	305	0.12	0.25	3.48 (0.39)	59.5	...	0.37 (6.54)	-0.23 (7.13)	-0.20 (5.69)
497	51989	73	0.20	0.40	1.12 (0.42)	38.6	-0.05 (24.50)	0.23 (2.12)
499	51988	152	0.11	0.29	1.81 (0.64)	49.7	0.0 (2.54)	0.76 (61.34)
511	52636	313	0.13	0.27	0.81 (0.37)	52.8	0.90 (4.77)
512	51992	302	0.05	0.23	1.26 (0.29)	44.3	...	-0.32 (1.72)	0.12 (2.86)	0.03 (3.82)
529	52025	408	0.02	0.17	...	0.0
550	51959	624	0.17	0.20	...	0.0	...	0.18 (78.96)
628	52083	262	0.03	0.12	...	0.0
629	52051	26	0.12	0.35	0.85 (0.34)	40.7	0.09 (2.35)	-0.20 (2.18)
637	52174	334	0.09	0.18	1.06 (0.46)	48.6	...	0.0 (1.67)	0.0 (4.10)	1.10 (2.86)
671	52206	347	0.04	0.28	4.23 (0.14)	24.2	...	0.0 (6.47)	-0.01 (2.07)	1.89 (13.63)
765	52254	179	0.04	0.21	...	0.0
782	52320	306	0.15	0.21	...	0.0	...	0.27 (1.36)
790	52441	527	0.03	0.14	1.83 (0.30)	67.3	0.0 (2.24)	-0.16 (4.21)
792	52353	432	0.14	0.20	1.76 (0.41)	23.1	...	0.13 (2.70)	-0.03 (2.03)	0.06 (2.04)
808	52556	39	0.21	0.37	...	0.0
845	52381	270	0.07	0.32	...	0.0
848	52669	602	0.05	0.22	2.22 (0.19)	42.0	-0.07 (1.91)	...
860	52319	451	0.04	0.16	1.66 (0.23)	32.5	0.0 (2.33)	0.29 (0.79)	0.41 (1.02)	0.23 (2.62)
864	52320	91	0.04	0.26	...	0.0	...	0.24 (1.81)	-0.24 (19.63)	-0.05 (2.01)
877	52353	458	0.04	0.06	...	0.0

Table 2—Continued

plate	mjd	fiber	z_{fg}	z_{bg}	R	Incl	τ_u	τ_g	τ_r	τ_i
882	52370	122	0.06	0.18	...(...)	0.0	...(...)	...(...)	...(...)	...(...)
883	52430	366	0.05	0.13	...(...)	0.0	...(...)	0.11 (4.58)	-0.07 (2.56)	-0.03 (6.10)
884	52374	242	0.04	0.17	...(...)	0.0	...(...)	...(...)	...(...)	...(...)
889	52663	408	0.06	0.16	...(...)	0.0	...(...)	...(...)	...(...)	...(...)
896	52592	463	0.03	0.11	2.49 (0.19)	45.8	0.0 (123.79)	0.37 (10.70)	0.16 (5.94)	0.09 (47.10)
913	52433	151	0.08	0.16	...(...)	0.0	...(...)	0.10 (1.79)	-0.02 (2.56)	...(...)
931	52619	84	0.18	0.28	...(...)	0.0	...(...)	...(...)	...(...)	...(...)
958	52410	194	0.15	0.31	4.49 (0.81)	36.3	...(...)	...(...)	-0.38 (2.72)	-0.62 (1.29)
970	52413	408	0.30	0.38	...(...)	0.0	...(...)	...(...)	...(...)	...(...)
980	52431	300	0.13	0.29	1.49 (0.20)	18.1	...(...)	-0.67 (2.25)	-0.07 (1.48)	-0.21 (1.76)
1000	52643	337	0.09	0.32	...(...)	0.0	...(...)	...(...)	0.27 (2.88)	0.22 (1860.97)
1006	52708	624	0.05	0.13	1.86 (0.24)	53.2	...(...)	0.0 (1.54)	0.40 (1.60)	0.28 (2.76)
1007	52706	519	0.05	0.20	...(...)	0.0	...(...)	...(...)	...(...)	...(...)
1160	52674	468	0.24	0.29	...(...)	0.0	...(...)	...(...)	...(...)	...(...)
1215	52725	288	0.27	0.33	...(...)	0.0	...(...)	-0.01 (1.73)	...(...)	...(...)
1230	52672	639	0.05	0.16	1.19 (0.37)	60.9	0.0 (2.30)	0.18 (2.21)	0.27 (2.85)	0.11 (125.74)
1235	52734	164	0.10	0.33	0.88 (0.24)	61.2	...(...)	-0.03 (1.94)	-0.20 (3.08)	0.13 (9.64)
1269	52937	485	0.03	0.19	...(...)	0.0	...(...)	0.01 (5.78)	...(...)	...(...)
1280	52738	125	0.08	0.21	...(...)	0.0	...(...)	...(...)	...(...)	...(...)
1282	52759	630	0.12	0.28	0.57 (0.26)	43.7	...(...)	0.0 (1.93)	0.44 (207.10)	0.26 (19.18)
1310	53033	202	0.11	0.18	...(...)	0.0	...(...)	...(...)	...(...)	...(...)
1317	52765	9	0.10	0.20	...(...)	0.0	...(...)	...(...)	...(...)	...(...)
1321	52764	461	0.15	0.22	2.14 (0.41)	35.4	...(...)	-0.50 (32.41)	-0.03 (3.15)	0.20 (1.73)
1324	53088	50	0.04	0.23	1.97 (0.32)	68.4	...(...)	-0.19 (2.20)	-0.03 (2.16)	-0.12 (2.98)
1325	52762	313	0.12	0.21	...(...)	0.0	...(...)	-0.02 (2.39)	...(...)	...(...)
1327	52781	252	0.08	0.14	...(...)	0.0	...(...)	...(...)	...(...)	...(...)
1332	52781	469	0.28	0.32	5.83 (0.64)	23.2	...(...)	...(...)	-1.09 (2.08)	-1.25 (2.37)
1363	53053	104	0.18	0.27	1.12 (0.38)	55.6	...(...)	0.0 (1.55)	-0.05 (9.05)	0.17 (7.07)
1373	53063	255	0.03	0.13	...(...)	0.0	0.0 (2.30)	...(...)	...(...)	...(...)
1390	53142	385	0.13	0.29	2.08 (0.49)	26.1	...(...)	...(...)	0.07 (2.41)	0.05 (1.68)
1416	52875	490	0.07	0.19	2.18 (1.17)	14.4	...(...)	-0.03 (1.77)	...(...)	...(...)
1423	53167	528	0.20	0.33	1.73 (0.50)	42.2	...(...)	...(...)	-0.54 (1.35)	-0.18 (1.77)
1429	52990	336	0.07	0.15	1.25 (0.16)	42.7	0.0 (2.61)	0.0 (2.78)	0.67 (1.63)	0.06 (2.11)
1604	53078	459	0.08	0.17	0.82 (0.43)	42.2	...(...)	0.94 (6.10)	0.49 (1.32)	1.61 (1.98)
1607	53083	48	0.08	0.15	...(...)	0.0	...(...)	-0.63 (6.30)	...(...)	...(...)
1618	53116	285	0.04	0.17	...(...)	0.0	...(...)	...(...)	...(...)	...(...)
1620	53137	175	0.07	0.10	1.00 (0.21)	47.7	0.0 (8.61)	-0.23 (1.69)	0.05 (5.04)	-0.17 (23.12)

Table 2—Continued

plate	mjd	fiber	z_{fg}	z_{bg}	R	Incl	τ_u	τ_g	τ_r	τ_i	τ_z
1677	53148	262	0.19	0.31	...(...)	0.0	...(...)	...(...)	...(...)	...(...)	...(...)
1746	53062	533	0.14	0.25	1.21 (0.38)	50.1	...(...)	0.39 (4.83)	0.80 (1.64)	0.36 (1.92)	-0.23 (...)

Table 3. The optical depths of the stacked SDSS filters. These values have not been corrected for inclination.

plate	mjd	fiber	z_{fg}	z_{bg}	R	τ_{gr}	τ_{ri}	τ_{iz}	τ_{gri}	τ_{griz}
267	51608	499	0.04	0.09	-0.13 (4.83)
273	51957	323	0.11	0.18
275	51910	233	0.03	0.09	0.80 (0.09)	...	0.30 (18.64)	0.05 (7.67)	0.31 (5.25)	0.05 (16.51)
281	51614	624	0.05	0.20
282	51658	120	0.07	0.26	1.52 (0.24)	...	-0.03 (1.43)	-0.00 (1.60)	...	0.00 (15.92)
285	51930	15	0.02	0.14
313	51673	546	0.04	0.30
367	51997	222	0.08	0.14
403	51871	586	0.14	0.17
408	51821	336	0.07	0.12	0.39 (1.45)
435	51882	118	0.23	0.26
436	51883	638	0.04	0.36	1.00 (0.18)	...	0.15 (15.17)	0.19 (6.96)	...	0.29 (8.28)
440	51885	370	0.18	0.25
464	51908	211	0.12	0.20
474	52000	548	0.21	0.30
484	51907	616	0.16	0.25
487	51943	305	0.12	0.25	3.51 (0.37)	...	-0.24 (1.80)	-0.09 (4.14)	...	-0.09 (3.63)
497	51989	73	0.20	0.40	1.27 (0.36)	...	0.04 (1.79)	0.10 (2.47)
499	51988	152	0.11	0.29	-0.42 (1.65)
511	52636	313	0.13	0.27	0.52 (2.55)	...	0.21 (1.04)	...
512	51992	302	0.05	0.23	0.98 (0.24)	...	0.00 (18.95)	-0.06 (26.34)	...	0.01 (17.92)
529	52025	408	0.02	0.17
550	51959	624	0.17	0.20
628	52083	262	0.03	0.12
629	52051	26	0.12	0.35	0.76 (0.30)	...	0.19 (1.66)	0.37 (11.43)
637	52174	334	0.09	0.18	1.12 (0.50)	...	0.00 (5.20)	0.22 (2.16)
671	52206	347	0.04	0.28	3.88 (0.14)	...	0.10 (2.09)	-0.33 (2.66)	...	-0.84 (2.07)
765	52254	179	0.04	0.21
782	52320	306	0.15	0.21
790	52441	527	0.03	0.14	-0.03 (1.43)
792	52353	432	0.14	0.20	1.88 (0.45)	...	0.15 (2.90)	0.07 (1.81)	...	0.08 (2.16)
808	52556	39	0.21	0.37
845	52381	270	0.07	0.32
848	52669	602	0.05	0.22	1.44 (0.16)	...	0.22 (1.84)	0.65 (1.67)	...	0.30 (1.71)
860	52319	451	0.04	0.16	1.54 (0.22)	0.35 (1.93)	0.28 (1.73)	0.37 (1.69)	0.37 (1.29)	0.42 (1.93)
864	52320	91	0.04	0.26	1.89 (0.25)	...	-0.17 (3.73)	-0.20 (3.50)	...	-0.05 (3.88)
877	52353	458	0.04	0.06

Table 3—Continued

plate	mjd	fiber	z_{fg}	z_{bg}	R	τ_{gr}	τ_{ri}	τ_{iz}	τ_{gri}	τ_{griz}
882	52370	122	0.06	0.18	...(...)	...(...)	...(...)	...(...)	...(...)	...(...)
883	52430	366	0.05	0.13	2.78 (0.55)	...(...)	-0.18 (17.96)	-0.09 (2.66)	...(...)	...(...)
884	52374	242	0.04	0.17	...(...)	...(...)	...(...)	...(...)	...(...)	...(...)
889	52663	408	0.06	0.16	...(...)	...(...)	...(...)	...(...)	...(...)	...(...)
896	52592	463	0.03	0.11	2.10 (0.20)	0.35 (2.16)	0.16 (6.66)	0.02 (2.51)	0.47 (1.58)	0.09 (4.17)
913	52433	151	0.08	0.16	...(...)	...(...)	-0.10 (1.79)	...(...)	...(...)	...(...)
931	52619	84	0.18	0.28	...(...)	...(...)	...(...)	...(...)	...(...)	...(...)
958	52410	194	0.15	0.31	4.08 (0.77)	...(...)	-0.55 (1.84)	0.04 (2.64)	...(...)	0.00 (1.03)
970	52413	408	0.30	0.38	...(...)	...(...)	...(...)	...(...)	...(...)	...(...)
980	52431	300	0.13	0.29	0.99 (0.28)	...(...)	0.00 (1.73)	-0.27 (115.35)	...(...)	-0.28 (11.09)
1000	52643	337	0.09	0.32	...(...)	...(...)	...(...)	...(...)	...(...)	...(...)
1006	52708	624	0.05	0.13	1.94 (0.25)	...(...)	0.39 (1.83)	0.21 (1.92)	...(...)	0.40 (38.38)
1007	52706	519	0.05	0.20	...(...)	...(...)	...(...)	...(...)	...(...)	...(...)
1160	52674	468	0.24	0.29	...(...)	...(...)	...(...)	...(...)	...(...)	...(...)
1215	52725	288	0.27	0.33	...(...)	...(...)	...(...)	...(...)	...(...)	...(...)
1230	52672	639	0.05	0.16	1.61 (0.48)	...(...)	0.09 (13.43)	0.08 (1.68)	...(...)	0.10 (1.29)
1235	52734	164	0.10	0.33	2.89 (0.71)	...(...)	0.03 (1.11)	-0.09 (2.04)	...(...)	-0.07 (3.27)
1269	52937	485	0.03	0.19	...(...)	...(...)	...(...)	...(...)	...(...)	...(...)
1280	52738	125	0.08	0.21	...(...)	...(...)	...(...)	...(...)	...(...)	...(...)
1282	52759	630	0.12	0.28	0.52 (0.29)	0.32 (4.08)	0.25 (2.51)	0.09 (3.18)	...(...)	0.12 (1.75)
1310	53033	202	0.11	0.18	...(...)	...(...)	...(...)	...(...)	...(...)	...(...)
1317	52765	9	0.10	0.20	...(...)	...(...)	...(...)	...(...)	...(...)	...(...)
1321	52764	461	0.15	0.22	4.61 (0.40)	...(...)	0.16 (1.95)	0.09 (6.27)	...(...)	0.00 (1.99)
1324	53088	50	0.04	0.23	1.29 (0.21)	...(...)	0.04 (129.61)	0.02 (11.83)	...(...)	0.00 (7.32)
1325	52762	313	0.12	0.21	...(...)	...(...)	...(...)	...(...)	...(...)	...(...)
1327	52781	252	0.08	0.14	...(...)	...(...)	...(...)	...(...)	...(...)	...(...)
1332	52781	469	0.28	0.32	3.87 (0.90)	...(...)	-0.99 (3.02)	-1.28 (21.59)	...(...)	-0.99 (1.44)
1363	53053	104	0.18	0.27	2.02 (0.44)	...(...)	0.25 (11.95)	0.21 (1.32)	...(...)	...(...)
1373	53063	255	0.03	0.13	...(...)	...(...)	...(...)	...(...)	...(...)	...(...)
1390	53142	385	0.13	0.29	1.17 (0.54)	...(...)	0.17 (4.26)	0.23 (4.71)	...(...)	...(...)
1416	52875	490	0.07	0.19	...(...)	...(...)	...(...)	...(...)	...(...)	...(...)
1423	53167	528	0.20	0.33	...(...)	...(...)	-0.31 (1.17)	...(...)	...(...)	...(...)
1429	52990	336	0.07	0.15	1.27 (0.15)	0.00 (4.62)	0.48 (2.55)	-1.11 (8.44)	0.97 (3.81)	0.78 (1.85)
1604	53078	459	0.08	0.17	0.90 (0.52)	...(...)	0.64 (8.19)	-0.04 (4.06)	...(...)	0.82 (1.06)
1607	53083	48	0.08	0.15	...(...)	...(...)	...(...)	...(...)	...(...)	...(...)
1618	53116	285	0.04	0.17	...(...)	...(...)	...(...)	...(...)	...(...)	...(...)
1620	53137	175	0.07	0.10	1.33 (0.29)	...(...)	-0.11 (3.35)	-0.11 (1.32)	...(...)	-0.07 (11.45)

·
·
·

Table 3—Continued

plate	mjd	fiber	z_{fg}	z_{bg}	R	τ_{gr}	τ_{ri}	τ_{iz}	τ_{gri}	τ_{griz}
1677	53148	262	0.19	0.31	...(...)	0.44 (2.03)	...(...)	...(...)	...(...)	...(...)
1746	53062	533	0.14	0.25	1.14 (0.35)	...(...)	0.68 (8.73)	0.44 (2.08)	...(...)	...(...)

Table 4. Exponential fit values to optimum aperture optical depths

filter	$0.01 < z < 0.1$			$0.1 < z < 0.2$		
	τ_0	h	rms	τ_0	h	rms
u	0.1	-1.8	0
g	1.4	3.9	1.0	0.3	-16.7	0.6
i	0.3	-70.3	1.2	0.2	-3.4	0.9
r	0.7	7.6	1.2	0.3	-7.2	0.8
z	0.4	-648.5	1.1	0.7	6.6	1.0

Table 5. Exponential fit values to visual aperture optical depths

filter	$0.01 < z < 0.1$			$0.1 < z < 0.2$		
	τ_0	h	rms	τ_0	h	rms
u
g	0.04	-1.0	1.0	0.4	17.8	0.6
i	0.1	-2.1	1.2	0.3	6.2	0.9
r	0.1	-3.8	1.2	2.1	0.5	0.8
z	0.3	-5.6	1.1	0.4	9.3	1.0

Table 6. Exponential fit values to visual aperture optical depths in the r+i

Redshift	τ_0	h	rms
$z < 0.01$	0.9	1.3	0.9
(arm)	0.8	2.3	0.9
(disk)	1.2	0.8	0.7
$0.01 < z < 0.1$	0.2	2.9	1.2
$0.1 < z < 0.2$	0.3	7.4	0.7